Rapid fabrication and screening of tailored functional 3D biomaterials

Journal Pre-proof

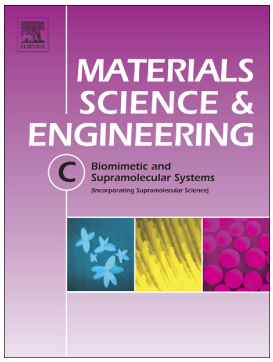

Rapid fabrication and screening of tailored functional 3D biomaterials

Antonio Conde-González, Deepanjalee Dutta, Robert Wallace, Anthony Callanan, Mark Bradley

PII: S0928-4931(19)32683-9

DOI: https://doi.org/10.1016/j.msec.2019.110489

Reference: MSC 110489

To appear in: *Materials Science & Engineering C*

Received date: 22 July 2019

Revised date: 9 November 2019

Accepted date: 23 November 2019

Please cite this article as: A. Conde-González, D. Dutta, R. Wallace, et al., Rapid fabrication and screening of tailored functional 3D biomaterials, *Materials Science & Engineering C* (2019), https://doi.org/10.1016/j.msec.2019.110489

Rapid Fabrication and Screening of Tailored Functional 3D Biomaterials

Antonio Conde-González[1], Deepanjalee Dutta[1], Robert Wallace[2], Anthony Callanan[3] and Mark Bradley[1,*]

[1]EaStCHEM School of Chemistry, University of Edinburgh, Edinburgh EH9 3FJ, UK

[2]Orthopaedics and Trauma, University of Edinburgh, Edinburgh EH16 4SB, UK

[3]School of Engineering, Institute for Bioengineering, University of Edinburgh, Edinburgh EH9 3DW, UK

[*]Corresponding author: Professor Mark Bradley (telephone 0131 650 1000) – mark.bradley@ed.ac.uk
The King's Buildings – The University of Edinburgh, West Mains road, Edinburgh EH9 3FJ, UK

Abstract

Three dimensional synthetic polymer scaffolds have remarkable chemical and mechanical tunability in addition to biocompatibility. However, the chemical and physical space is vast in view of the number of variables that can be altered e.g. chemical composition, porosity, pore size and mechanical properties to name but a few. Here, we report the development of an array of 3D polymer scaffolds, whereby the physical and chemical properties of the polymer substrates were controlled, simultaneously examined (e.g. parallel micro-CT scanning of 24 samples) and biological properties screened. This approach allowed the screening of 48 different polymer scaffolds constructed *in situ* by means of freeze-casting and photo-polymerisation with the tunable composition and 3D architecture of the polymer scaffolds facilitating the smart design of 3D biomaterials. As a proof of concept, the array approach was used to identify 3D polymers that were capable of supporting cell growth and control their behaviour. Sitting alongside classical polymer microarray technology, this novel platform reduces the gap between the identification of a biomaterial in 2D and its subsequent 3D application.

Keywords

3D biomaterials, scaffolds, pores, in vitro bone model, high-throughput.

Graphical abstract

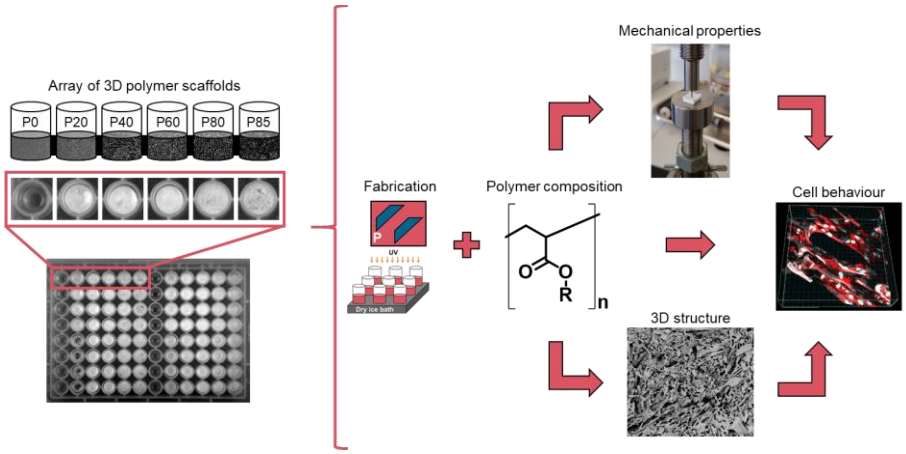

1. Introduction

To enable in vitro tissue engineering cells must be grown and organized in an environment that is capable of providing the correct geometry and mechanical properties, along with the necessary biological cues [1]. Traditional 2D culture systems, where cells adhered to a flat surface in a monolayer, unfortunately fail to provide the requisite environment and have been shown to alter the genetic and biochemical makeup of the cultured cells [2]. Thus functional biomaterials should mimic the native tissue microenvironment (e.g. natural 3D structure of tissues) and promote the formation of new tissue [3]. However, native tissues are highly complex and their unique properties are the result of the complex interplay between composition and the 3D arrangement of the extracellular matrix [4]. In addition, physical signals such as material stiffness and wettability or chemical signals from incorporated bio-inspired materials all have been shown to be capable of triggering cell signalling and directing cell fate [5–10]. For instance cell density in a biomaterial can be controlled using a polymer composition gradient leading to fabrication of tissue-like structures [11]. 3D hydrogels and scaffolds have been explored in order to simulate the complexity of native tissues [12,13]. As an illustration hydrogel scaffolds composed of different ratios of chitosan and poly(ethylenimine) were used to expand human skeletal stem cells mirroring the tissue 3D architecture [14]. However, despite of the incessant efforts made towards understanding the combined effects of a biomaterial inducing physical and chemical signals in modification of cellular fate, predicted outcomes nevertheless remain vague, attributed to the highly complex and concomitant and interwoven nature of processes involved.

Since the concept of combinatorial chemistry was introduced, the high-throughput synthesis and screening of synthetic polymers has developed in an attempt to understand both cell–material interactions and to discover functional biomaterials for specific biomedical applications [15,16]. For instance, the high-throughput screening of more than 7,000 polyacrylates allowed the identification of substrates that were capable of controlling human embryonic stem cells [17]. However, current polymer microarrays typically lack the defined 3D structures and morphologies that are present within tissues, and as such prevent direct translation, ultimately giving rise to aberrant cell behaviour. Among the various alternatives that have tried to shine light on this complex microenvironment, arrays of 3D biomaterials have been touted as a powerful tool to hasten the design and identification of new functional biomaterials [18,19]. For example, arrays of synthetic 3D hydrogels have been developed to study the effect of mechanical properties on cell fate [20], with gas foaming successfully used to generate an array of poly-L-lactic acid based materials where the microstructure of the polymer could be tuned [21]. Moreover, the adhesion of osteoblasts was also shown on a porous array of tyrosine-derived polycarbonates constructed through solvent casting and particulate leaching in a 96-well plate [22]. Arrays of 3D biomaterials have been shown to allow the achievement of more realistic in vitro cell culture models for a variety of applications like tissue repair, high-throughput drug screening, assay validation to name but a few. [23].

Porous polymer scaffolds are known to promote cell adhesion and migration in the scaffolds, which turns out to be instrumental in controlling cellular functions further facilitating tissue growth. Among the possible options that could be explored to generate arrays of porous polymers, freeze-casting offers a number of advantages with respect to the characteristics of the porous structure and mechanical properties. Prototyping technologies like 3D printing/bioprinting and electrospinning are material-dependent approaches where the printability of the material determine its applicability rather than its cellular response. Freeze-casting can also develop a better porous structures compared to other commonly used particulate leaching techniques where there can be aggregation of salt particles leading to variation of final pore size and poor interconnections [24]. Additionally, by applying cooling gradients and variation of both concentration or type of the porogenic solvent it allows precise control of morphologies as well as access to libraries of materials [25–27]. In a previous report the orientation and type of porous structure as well as its mechanical properties were controlled by modification of the templating temperature within pectin foams [28]. Considering these aspects, a high-throughput screening platform compatible with conventional cell culture plates to allow rapid identification of functional porous biomaterials is essential and would help to unlock the promise of combinatorial screening of novel 3D functional polymers.

To address the above, herein we report the development and characterisation of an array of 3D polymer scaffolds that expands the current available chemical and physical space of 3D biomaterials. The aim was to design and put into practise a robust, practical, approach to fabricate 3D polymer scaffolds with a variety of synthetic polymers, while offering a wide range of mechanical properties and 3D microstructures meticulously designed to be compatible with standard cell culture plates. Our method exploited freeze-casting and photo-polymerisation to allow the in situ fabrication of arrays of multi-material and multi-structure 3D scaffolds. In order to test the applicability of the approach developed, the array was explored to identify 3D biomaterials capable of replicating the properties of bone tissue. The developed platform, moreover, can be explored in a wide range of applications such as biomaterial-cell interface studies, personalised tissue repair, biochemical assays and pre-clinical drug screening. This new method, thereby, smooths the gulf between the identification of polymeric biomaterials in *classic* 2D culture and their transition to 3D models.

2. Materials and methods

2.1. Materials

2-(Methylthio)ethyl methacrylate (MTEMA), butyl methacrylate (BMA), isobornyl acrylate (IBA), ethylene glycol dicyclopentenyl ether acrylate (EGDPEA), 1,6-hexanediol diacrylate (HDOBA), 2-hydroxy-2-methylpropiophenone (PI) and Dulbecco's modified Eagle medium (DMEM) were purchased from Sigma-Aldrich. 4-tert-butylcyclohexyl acrylate (BHA) was obtained from Tokyo Chemical Industry (TCI). L-glutamine, fetal bovine serum (FBS), alamarBlue™ and DAPI (62248) were purchased from Thermo Fisher Scientific. A Live/Dead cell imaging assay and Alexa Fluor™ 568 phalloidin (A12380) were purchased from Invitrogen. 96-well plates made of polypropylene (flat bottom) were obtained from Greiner.

2.2. Preparation of the arrays of polymer scaffolds and characterization

2.2.1. Fabrication of arrays of 3D polymer scaffolds

The array of 3D polymer scaffolds was the result of photo-polymerisation using different porogenic solutions at sub-zero temperatures in 96-well plates. The porogenic solutions (80 µL/well) were obtained by a combination of the porogenic solvent (DMSO) and the polymerisation mixture - the polymerisation mixtures being composed of the photo-initiator (2-hydroxy-2-methylpropiophenone, 10% mol), the cross-linker (1,6-hexanediol diacrylate, 18% mol) and the appropriate combination of acrylate monomers (72% mol) (Table S1 and Fig. S1).

After the desired cooling stages, the arrays were UV cured (UV cross-linker CL-1000L 8W, 365 nm, 30 min) on top of a dry ice bath (Fig. S2) to maintain the solutions in frozen form. Following polymerization all the scaffolds were washed with ethanol and water (1:1, 2 days) and water (2 days) at 37 ºC before freeze-drying (2 days).

2.2.2. Structural analysis of the array of 3D polymer scaffolds using SEM.

Polymer scaffolds on the array were coated with gold/palladium alloy (3:2) employing a sputter coater (30 mA, 0.75 Torr). Image acquisition was performed using a Hitachi S-4700 with analysis of the scaffold morphology performed using ImageJ-Fiji (Fig. S6). Firstly SEM images were binarized and filtered to the porous structure from the polymer network. Subsequently the pores were characterised using the particle analyse plugin. Pores were quantified as porosity (percentage of scaffold's surface area covered by pores) and Feret's diameter (the maximum distance between the edges of the pore).

2.2.3. Structural analysis of the array of 3D polymer scaffold using micro-CT.

Sections of the array of 3D polymer scaffolds were arranged in a 2x2 matrix and stacked three rows high to form a cuboid of 2x2x3 wells and secured into a custom polystyrene sample holder to prevent movement during scanning. The sample holder was then mounted in a Skyscan 1172 desktop micro CT (Bruker, Kontich, Belgium) and scanned through 360 degrees using a step of 0.48 degrees between exposures. A voxel resolution of 5.94 µm was obtained using the following micro CT parameters: 34 kV source voltage, 210 µA source current with an exposure time of 1767 ms. Four frames were taken at each position and averaged to reduce noise. After scanning, the data was reconstructed using Skyscan NRecon v1.6.9 (Bruker, Kontich, Belgium). A reconstruction thresholding window of 0.00 to 0.05 in CT attenuation coefficient with no beam hardening correction was used.

Volume of interests (VOI) of the reconstructed micro-CT scans were binarized and porosity of the scaffolds was analysed using Fiji-BoneJ [29]. Analysis of the porous network in polymers with large porosity (P60, P80 and P85) were then implemented using CTAn v1.16.4 (Bruker, Kontich, Belgium). A circular region of interest 4.75 mm diameter was extended 0.62 mm (± 0.19 SD) through the

structure to define the VOI. After that, a greyscale threshold range of 52 - 255 was applied to the VOIs to obtain the binary structure, all speckles smaller than 4 pixels were removed, and then 3D morphological analysis was carried out to determine; polymer thickness, connectivity density of the polymer structure, pore diameter and open porosity.

2.2.4. Mechanical characterisation of the polymer scaffolds using macro-indentation.

Scaffolds were fabricated at low porosity (P0), medium porosity (P60) and high porosity (P80) by the slow cooling templating approach. The porogenic solutions (300 µL) were UV polymerised (UV cross-linker CL-1000L 8W, 365 nm, 60 min) at sub-zero temperatures in polystyrene moulds (12 mm x 12 mm). After washing and drying, the scaffolds were re-hydrated for 2 days before mechanical characterisation (Fig. S13). Polymer scaffolds were tested using an Instron testing system (model 3367) equipped with the software Bluehill 3 (Norwood, USA), a 50 N load cell for compression and a flat cylindrical indenter (ø = 1 mm) made in house. The height of the samples was taken using a digital Vernier calliper (1.7 mm). The samples were compressed at a strain rate of 5% per minute for 20% of the strain. The relaxation load was measured for 5 min. The indentation modulus was calculated locally between 0% and 5%, 5% and 10%, 10% and 15% and 15% and 20% of the strain using a linear model for semi-infinite media (diameter sample to diameter indenter ≥ 3) in 3D samples previously described [30–32]. The relaxation load (%) is described as the reduction of load after 1 min and 5 min of relaxation [33,34].

2.3. In vitro evaluation

2.3.1. Cell morphology on the array of 3D polymer scaffolds using SEM

Sarcoma osteogenic (SAOS-2, ATCC HTB-85) cells were cultured and expanded to confluence in complete culture medium (DMEM supplemented with 10% FBS, 1% L-glutamine and 1% penicillin/streptomycin) before seeding on the 3D scaffolds. The polymers were UV sterilized overnight and pre-conditioned with 50 µL of culture medium for 1 hour before cell seeding. A suspension of the cells was seeded in the polymer scaffolds (20,000 cells in 150 µL). The cells were incubated in the scaffolds at 37 °C and 5% CO_2 in a humidified atmosphere for 3 days. The incubation media was removed, scaffolds were washed with PBS (100 µL, 10 min) and cells were fixed with paraformaldehyde (4%, 15 min). After fixation, sodium cacodylate buffer (0.1 M, 1 hour) was used to remove excess PFA. Polymer scaffolds were removed from the wells and osmium tetroxide (0.1M, 45 min) used for post-fixation. After further washing with sodium cacodylate buffer (0.1M, 15 min), the scaffolds were dehydrated in different concentrations of acetone (50%, 70%, 90% and 100%) and critical point drying (liquid CO_2). The specimens were coated with a gold/palladium alloy and image acquisition was obtained using a Hitachi S-4700 scanning electron microscope (SEM).

2.3.2. Cell viability in the array of 3D polymer scaffolds

Arrays of 3D polymer scaffolds were fabricated using 8 different polymers (1 - 8) with 6 levels of porosity (P0, P20, P40, P60, P80 and P85) using the slow cooling approach (Fig. S10). The arrays were UV sterilized overnight and pre-conditioned with 50 µL of complete culture medium before adding a suspension of SAOS-2 cells (20,000 in 150 µL). Medium was changed every two days.

Metabolic activity of SAOS-2 in the 48 polymer scaffolds was assessed at day 1, 3 and 7 with amarBlue™. At the appropriated time, culture media was removed and 100 µL of the solution of alamarBlue™ in basal media (10 % v/v) was incubated for 4 hours (37 °C, 5% CO_2) in the polymer scaffolds. Subsequently, the supernatant was collected and fluorescence intensity was recorded using a microplate reader (ex/em 530/590). The arrays were washed with PBS and complete media added to maintain the cells in culture until the next time point. The fluorescence readings were normalized to the results obtained in a standard 96 tissue culture well plate (TC) with day 1 used as a reference.

2.3.3. Live/dead staining in the array of 3D polymer scaffolds

Sarcoma osteogenic (SAOS-2) cells were seeded in a suspension of basal media (20,000 SAOS-2 in 150 µL) and incubated in sterilised arrays of polymer scaffolds in a humidified atmosphere (37 °C and 5% CO_2) with media changes every two days. The live/dead cell imaging kit composed of calcein AM (ex/em 488/512 nm) for living cells and a nuclear red fluorescence dye (ex/em 570 nm/602 nm) for dead cells was performed at day 7. Image capturing in 3D was performed using a Nikon Eclipse 50i microscope and the Pathfinder™ software (IMSTAR, France).

2.3.4. Cytoskeleton staining in the array of 3D polymer scaffolds

Sarcoma osteogenic (SAOS-2) cells were seeded on the array of 3D polymer scaffolds following the procedure previously described. After 7 days of incubation, arrays were washed with PBS and cells were fixed (4% PFA, 15 min). Prior to nucleus and actin staining, fixed SAOS-2 cells were permeabilized (0.1% Triton X-100 in PBS, 15 min) and washed with PBS (10 min). Cell nuclei were stained using a solution of DAPI (5 µg/ml) in PBS for 10 min (100 µL/scaffold). After removing the DAPI working solution and washing the scaffolds with PBS (10 min), the actin cytoskeleton was stained with Alexa Fluor™ 568 phalloidin (1:40 dilution) for 30 min at room temperature. After three washing cycles, scaffolds were extracted from the 96-well plate, sectioned and mounted on a glass slide. Z-stack fluorescence images were obtained using a confocal microscope Zeiss LSM880 Airscan equipped with a 20X NA 0.8 air objective. Cytoskeleton orientation was evaluated with the Imagej plugin OrientationJ [35].

2.4. Statistical analysis

Results are presented as mean ± SD. Statistical significant differences were evaluated by two-way ANOVA or one-way ANOVA followed by Bonferroni's post-test. A $p < 0.05$ was considered statistically significant. Three independent biological experiments with three technical replicates were accomplished for each experiment unless otherwise indicated.

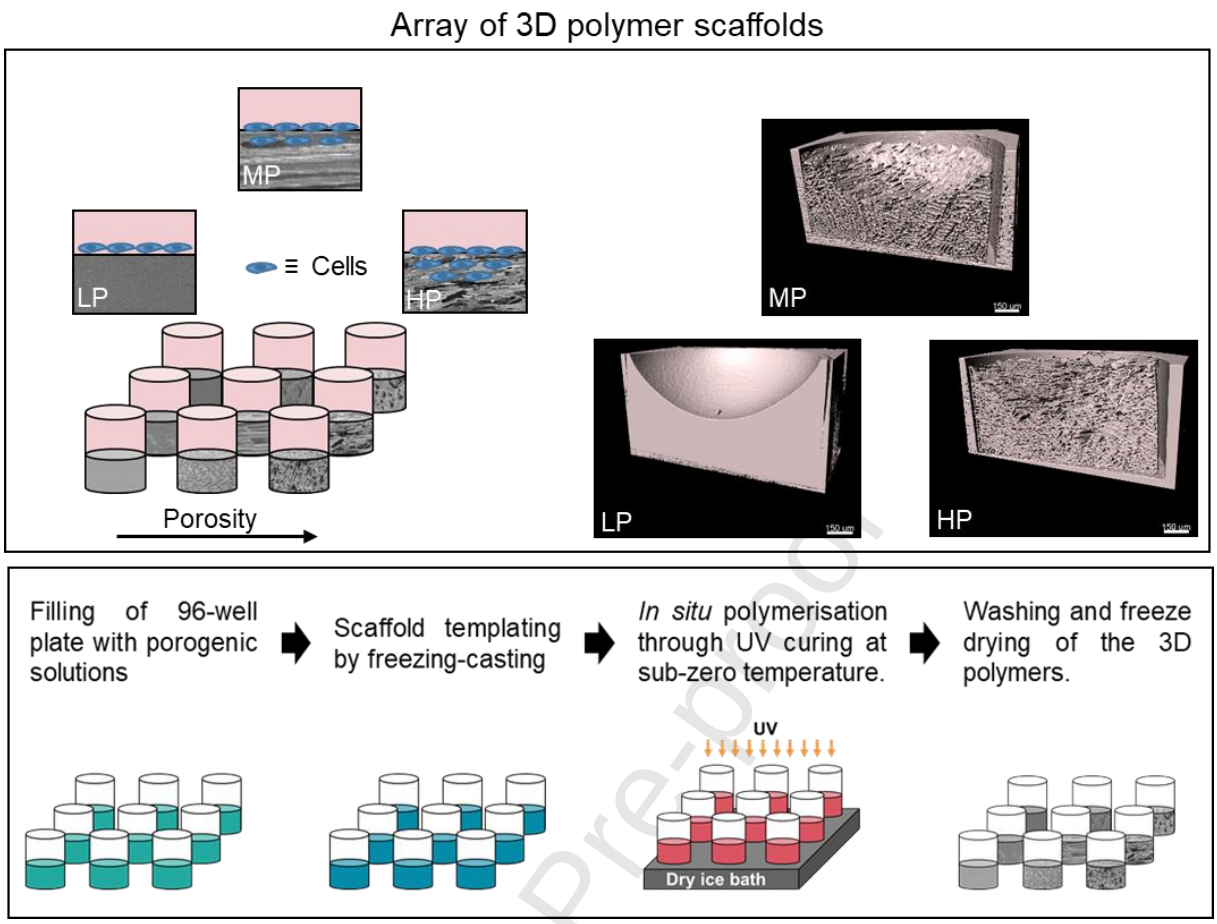

Figure 1. An array of 3D polymer scaffolds. *Low porosity (LP or low concentration of porogenic solvent i.e. P0 and P20), medium porosity (MP or medium concentration of porogenic solvent i.e. P40 and P60) and high porosity (HP or high concentration of porogenic solvent i.e. P80 and P85) scaffolds were constructed using a multi-component approach to allow the identification of suitable 3D biomaterials for cellular applications. A four-step process was designed to tune in situ the microstructure and mechanical properties of the polyacrylates. The arrays of polymer scaffolds were prepared in standard 96-well plates to ensure applicability within a laboratory setting.*

3. Results

3.1. Development of arrays of porous polymer scaffolds and their characterization

3.1.1. Fabrication of arrays of 3D polymer scaffolds

The arrays of 3D polymer scaffolds were obtained by photo-polymerisation of the appreciate polymerisation mixture with various levels of porogenic solutions at sub-zero temperatures in standard 96-well plates (Fig. 1). Below the melting point of DMSO (19 °C) phase separation of the porogenic solutions produced a phase rich-in-monomers and a phase rich-in-solvent. The subsequent polymerisation, washing and drying of the plates generated the polymer scaffolds. In the present work acrylate-based monomers were explored for the fabrication of the polymer scaffolds (Table S1 and Fig. S1). Previous reports demonstrated that polyacrylates allowed the engineering of a broad range

of tissues [36–38] with the acrylate polymers employed here having been shown to promote the adherence and growth of human embryonic stem cells [17].

The fabrication of the arrays of the 3D polymer scaffolds were optimised and the materials were physically characterised for four representative polymer compositions with varying quantities of porogenic solvent (DMSO) in order to comprehend the solvent's effect on the 3D structure of the scaffolds. Subsequently biological response was assessed across the entire array to discover the polymer that showed optimal cell behaviour.

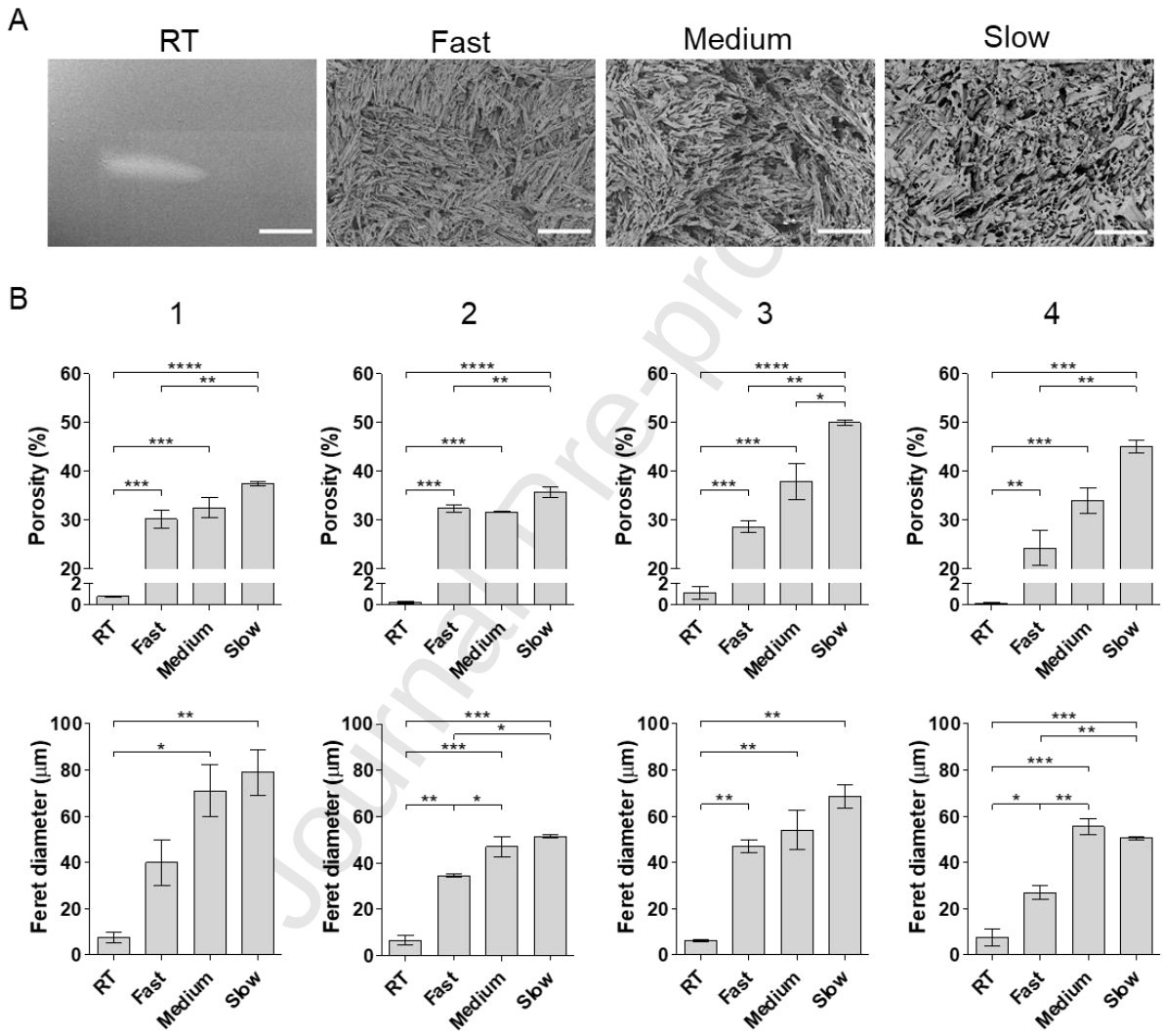

Figure 2. Effect of the templating temperature on the polymer scaffolds. *A) SEM images of the porous structure with different cooling procedures (using polymer 2). B) Analysis of the effect of the cooling procedure on the porosity (%) and ferret diameter (µm) of polymers 1, 2, 3 and 4. One-way ANOVA with Bonferroni post-test (* p ≤ 0.05, ** p ≤ 0.01, *** p ≤ 0.001 and **** p ≤ 0.0001). Mean ± SD, n=2. Scale bar 500 µm.*

3.1.2. Effect of the cooling gradient on the scaffold structure

The cooling gradient was first optimised on scaffolds with high porosity (80% v/v DMSO and 20% polymerisation mixture (named P80) with polymers 1, 2, 3 and 4 (Table S1 and Fig. S1). These four polymers were chosen as representative of the entire array, additionally, scaffolds with a large porosity (P80) were chosen to realize the effect of the cooling gradient on large pores. Four different templating temperatures were explored, so-called fast cooling, medium cooling, slow cooling and no cooling (polymerisation at room temperature). Fast cooling was achieved by freezing the samples on an aluminium cooling block (Fig. S2) on top of a dry ice bath (– 80 °C for 15 min). Medium cooling was attained by cooling the samples in a freezer (– 20 °C for 20 hours). Slow cooling was a two steps process where the scaffolds were cooled first in a fridge and subsequently cooled in a freezer (5 °C for 16 hours and – 20 °C for 4 hours respectively) and photopolymerised on dry ice. As a control, the effect of polymerizing at room temperature was also explored. Quantification of cooling gradients (Fig. S4) showed that the fast cooling gradient was 15.6 °C/min while medium cooling gradient was 2.5 °C/min. Slow cooling was divided in two steps, where the first step had a cooling gradient of approximately 1 °C/min while second step had a cooling gradient of 2.6 °C/min.

Illustrative SEM images of scaffolds fabricated at room temperature (no crystallization in the porogenic solvent) showed a surface exempted of large pores, whereas the surface of scaffolds after a cooling procedure showed a highly porous surface (Fig. 2A). Moreover, an increase in the size of the pores was observed when the cooling gradient was altered from “fast to slow”.

Quantification of these observations was performed using Imagej-Fiji (Fig. 2B). Porosity (%) as the percentage of the scaffold covered by pores and Feret’s diameter of those pores (µm) were used to analyse the 3D structure of the polymers. The polymers all exhibited an increase in porosity when a cooling procedure was applied. The porosity of P80-1 with and without a freezing stage were 30% higher and 1% lower respectively ($p \leq 0.001$). Similarly the other P80 scaffolds showed the same trend; with porosities higher than 30% and lower than 0.5% ($p \leq 0.001$) for P80-2, higher than 28% and lower than 2% ($p \leq 0.001$) for P80-3 and higher than 24% and lower than 0.5% ($p \leq 0.01$) for P80-4. Moreover, the porosity was also greater when the cooling gradient was changed from “fast to slow”. The porosity for P80-1 was 30 ± 2% and 38 ± 1% between “fast cooling” and “slow cooling” ($p \leq 0.05$). P80-2 scaffolds made with fast and slow cooling exhibited porosities of 32 ± 1% and 36 ± 1% ($p \leq 0.05$) respectively. P80-3 and P80-4 changed from 29 ± 1% to 50 ± 1% ($p \leq 0.01$) and from 24 ± 4% to 45 ± 1% ($p \leq 0.01$).

Significant differences were observed in the size of these pores when the polymerisation was carried out in the absence or presence of a cooling stage. The Feret’s diameter for P80-1 scaffolds fabricated at room temperature or with fast and slow cooling were 8 ± 2 µm, 40 ± 10 µm and 79 ± 10 µm respectively. Significant differences were also observed between “room temperature” and “slow cooling” ($p \leq 0.01$) as well as between “fast” and “slow cooling” ($p \leq 0.05$). Similar trends were observed for P80-2, P80-3 and P80-4. Feret’s diameter for P80-2 scaffolds were 7 ± 2 µm, 34 ± 1 µm

and 41 ± 1 µm for room temperature and fast and slow cooling respectively. P80-3 and P80-4 scaffolds were 6 ± 1 µm, 47 ± 3 µm and 69 ± 5 µm and 7 ± 4 µm, 27 ± 3 µm and 51 ± 1 µm.

Overall, reducing the cooling gradient produced an increase of the porosity and the size of these pores. The "slow cooling" (5 °C for 16 hours and – 20 °C for 4 hours) approach was selected in the view of maximising the porous nature of the scaffolds.

3.1.3. Effect of the porogenic solvent on the scaffold structure

The effects of the concentration of DMSO on the 3D porous structure were analysed using SEM. Four polymer compositions (using polymers 1, 2, 3 and 4) and three concentrations of DMSO were explored to construct polymer scaffolds with low (P0), medium (P60) and high (P80) porosity. The arrays were prepared with the slow cooling method (5 °C for 16 hours and – 20 °C for 4 hours) and polymerisation (UV, 30 min) was carried out as described above.

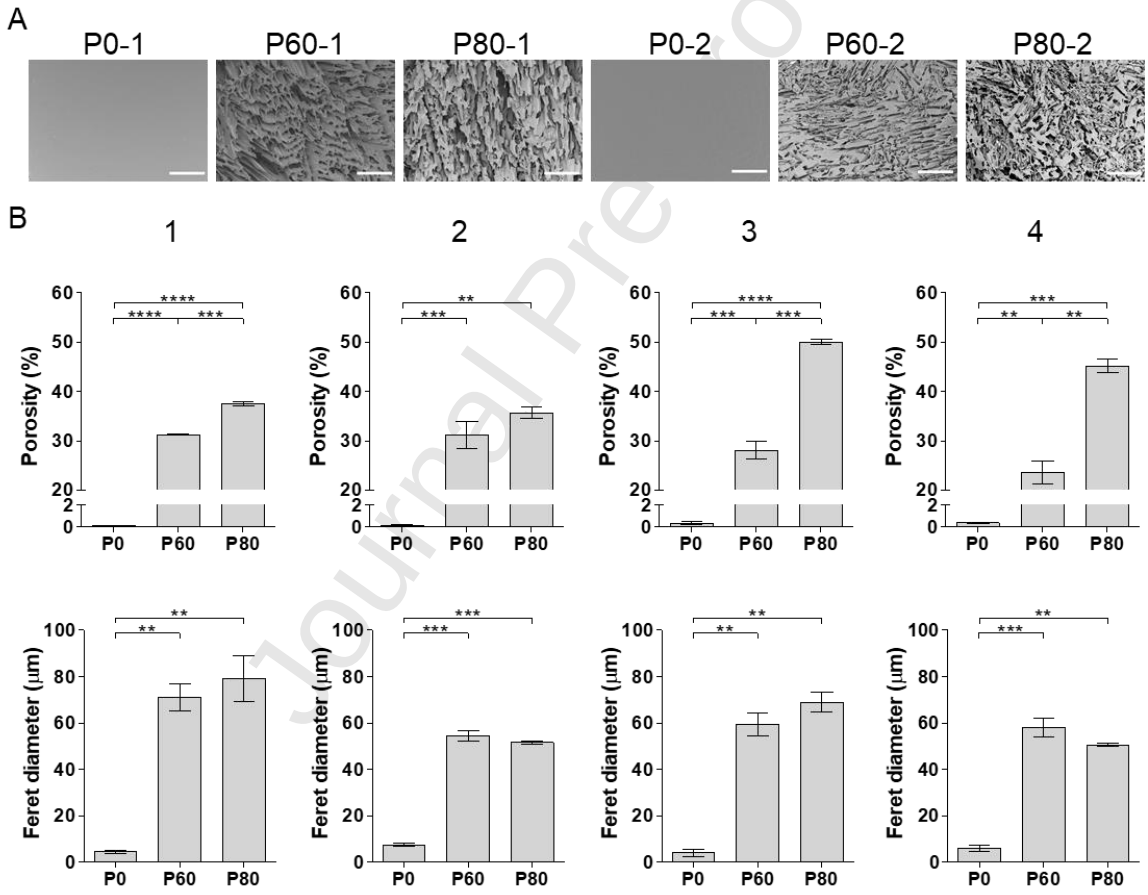

Figure 3. Effect of the level of porogenic solvent on the polymer scaffolds. *A) SEM images of the porous structure at different concentrations of porogenic solvent for polymers 1 and 2. B) Analysis of the effect of the concentration of DMSO on the porosity (%) and ferret diameter (µm) of the polymers 1, 2, 3 and 4. Mean ± SD, n=2. One-way ANOVA with Bonferroni post-test (* p ≤ 0.05, ** p ≤ 0.01, *** p ≤ 0.001 and **** p ≤ 0.0001). Mean ± SD, n=2. Scale bar 500 µm.*

Representative SEM images of polymers 1 and 2 with low, medium and high concentration of DMSO illustrated how the porous structure is altered when the concentration of DMSO is modified (Fig. 3A). Images revealed the absence of pores when porogenic solvent (DMSO) was absented and the presence of an ever increasing porous structure when the concentration of DMSO increased.

Quantitative analysis of the porous structure was performed using Imagej-Fiji (Fig. 3B). Generally the porosity of the scaffolds rose progressively when the concentration of DMSO increased from P0 (0% DMSO) to P80 (80% DMSO). For example the porosity between P0-1 and P60-1 changed from approximately 1% to 31 ± 1 ($p \leq 0.0001$) and increased to 38 ± 1 ($p \leq 0.001$) for P80-1. The same trend was observed for the other polymers, in the case of P0-2, P0-3 and P0-4 their porosity was lower than 1%, rising to 31 ± 3 ($p \leq 0.001$), 28 ± 2 ($p \leq 0.001$) and 24 ± 2 ($p \leq 0.01$) for P60-2, 3 and 4 respectively. Further increase of the porosity was observed for P80-2, 3 and 4, which reached 36 ± 1, 50 ± 1 ($p \leq 0.001$) and 45 ± 1 ($p \leq 0.01$) respectively.

A significant increase of the Feret's diameter was also observed between the scaffolds with low porosity (P0) and the scaffolds with medium and high porosity (P60 and P80). For example the Feret's diameter changed from 5 ± 1 µm for P0-1 to more than 70 µm for P60-1 and P80-1 ($p \leq 0.01$). In the case of P0-2, P0-3 and P0-4 their Feret's diameter was 6 ± 1 µm, 4 ± 1 µm and 6 ± 1 µm respectively, increasing to more than 50 µm for P60-2 and P80-2 ($p \leq 0.001$), 60 µm for P60-3 and P80-4 ($p \leq 0.01$) and 50 µm for P60-4 and P80-4 ($p \leq 0.01$).

Generally, increasing the concentration of DMSO (from P0 to P80) generated more pores (porosity) with larger size (Feret's diameter).

3.1.4. 3D morphological analysis of the array of 3D polymer scaffolds

Deeper understanding of the morphological characteristics of the array of polymer scaffolds was gained using micro-CT (Fig.4). The array of 3D polymer scaffolds was prepared with the slow cooling procedure where 4 polymer compositions (polymers 1, 2, 3 and 4) and increasing concentrations of porogenic solvent (DMSO) from 0% to 85% v/v (giving so-called scaffolds P0, P20, P40, P60, P80 and P85) were combined to give 24 individual porous polymers. Analysis was performed independently of the polymer composition to focus on the effect of the concentration of DMSO on the polymer structure.

Representative stacks of the longitudinal and cross-section for polymer 4 illustrates the reduction of polymer density through the increase of porogenic solvent (Fig.4A). Moreover, the 3D rendering of the longitudinal section of P80-2 showed that the polymer scaffold filled the entire volume of the well (Video S1 and Fig. 4B). Analysis of the CT data (with Imagej-Bonej) of the scaffold array showed the effect of increasing the levels of DMSO on the scaffolds porosity, independent of the polymer composition (Fig. 4C). For example, P20 (20% DMSO and 80% polymerisation mixture) showed an average porosity of 19 ± 7% whereas for P60 was 63 ± 6%. The largest porosity was achieved for P80 and P85 at 81 ± 6% and 84 ± 5% respectively.

Further analysis of the characteristics of the porous structures (with CTAn v1.16.4) was performed on the scaffolds with medium porosity (P60) and high porosity (P80 and P85) for the four-model polymers. These range of porosities have found to be more relevant in the fabrication of tissue 3D models for bones [6,39]. Polymer thickness (diameter of the greatest sphere that fits within the polymer structure), polymer connectivity (connected structures through the Euler characteristic), pore diameter (diameter of the greatest sphere that fits within the pore) and open porosity (pores connected to the out layer of the volume of interests) were used to characterise these 3D materials. The P60 scaffolds gave a broad range of "polymer thickness" (44.7 ± 14.8 µm) whereas, not unexpectedly the P80 and P85 scaffolds showed only small differences in form between them (37.6 ± 2.7 µm and 34.4 ± 3.2 µm) (Fig. 4D - i). The polymer connectivity density showed the interconnection of the polymer structure in the scaffolds (Fig. 4D – ii). The lowest polymer "connectivity" was for the P80 scaffolds (965 ± 563 mm^{-1}) while the average of the polymer connectivity for P60 and P85 were slightly larger (3210 ± 1322 mm^{-1} and 2713 ± 942 mm^{-1} respectively) for the four polymer composition considered. Overall, polymer thickness and connectivity decreased when ratio of porogenic solution to polymerisation mixture increased.

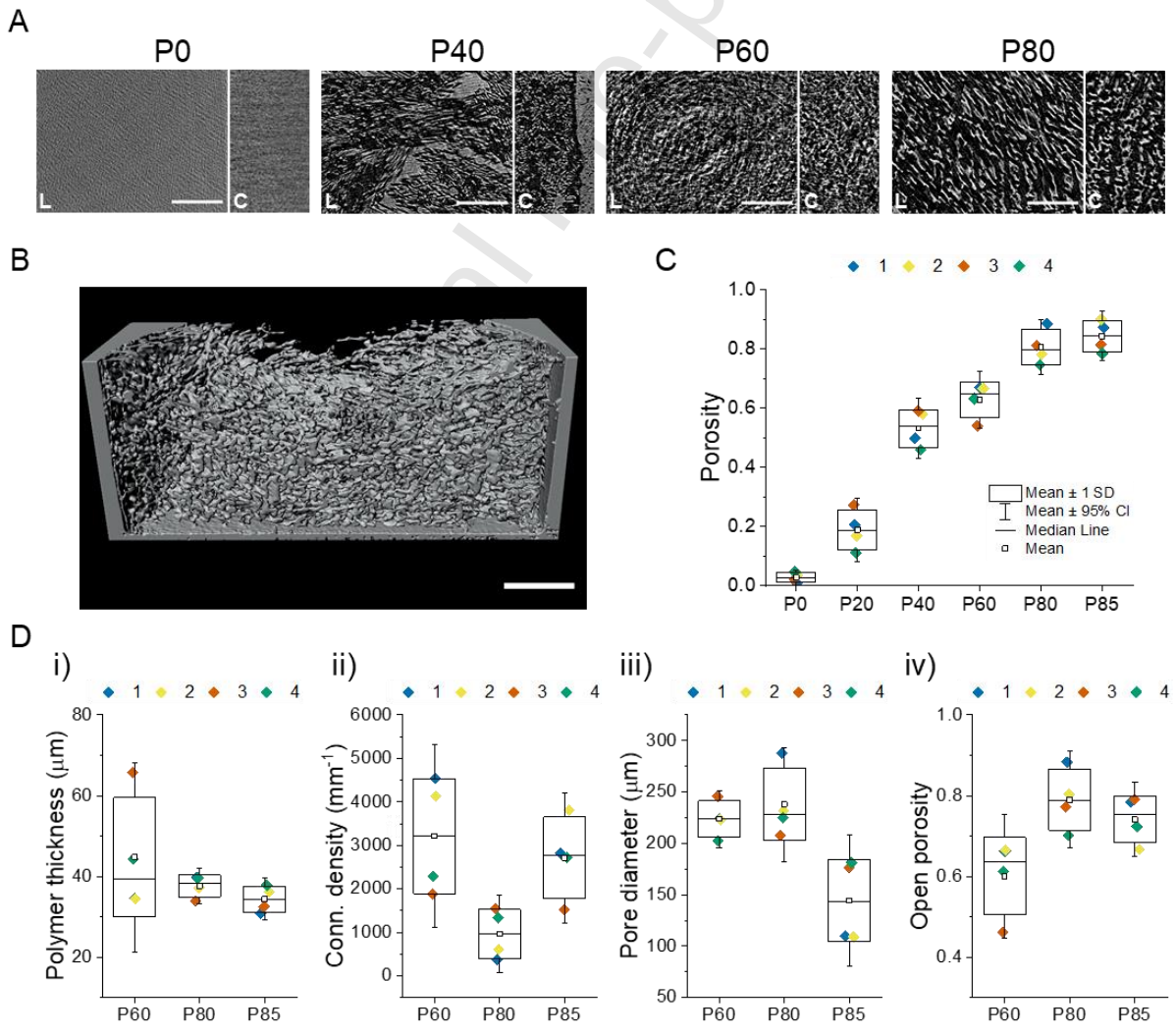

Figure 4. Analysis of the 3D structure of the porous scaffolds. *A) Representative images of longitudinal section (L) and cross-section (C) of polymer 4 fabricated using different levels of DMSO (P0, P40, P60 and P80). As shown the polymer is white and grey and pores are shown in black. Scale bar 1 mm. B) 3D rendering of the longitudinal section of polymer 2 high porosity (P80). Scale bar 1 mm. C) Analysis of the effect of the porogenic solvent (from 0% DMSO to 85% DMSO) on the porosity for polymers 1, 2, 3 and 4 using Fiji-Bonej. D) Characterisation of the polymers 1, 2, 3 and 4 with medium (P60) and large porosity (P80 and P85) using CTAn. Average of thickness of the polymer (µm), connectivity density of the polymer (mm^{-1}), diameter of the pores (µm) and open porosity were used to analyse the polymer network and porous structure.*

The diameter of the pores for the scaffolds P60, P80 and P85 was also analysed independently of the polymer composition (Fig. 4D – iii). The diameter of the pores was found to be similar for P60 and P80 (223.7 ± 17.6 µm and 238.1 ± 34.9 µm respectively). However, for the largest levels of porogenic solvent (P85) there was a reduction in the size of the pores for all polymers. The open porosity or porosity open to the surface of the volume of interest was used as a representation of the interconnectivity of the porous network (Fig. 4D-iv). The highest values were obtained for the P80 scaffolds whereas the P60 and P85 scaffolds were slightly lower (82 ± 5%, 60 ± 12% and 75 ± 7% respectively).

In the particular case of scaffolds P60 and P80 of polymers 1 and 2, the open porosity increased from 66% to 88% (P60-1 and P80-1) and 67% to 80% (P60-2 and P80-2). The diameter of the pores for the same polymers also increased from 224 µm to 288 µm (P60-1 and P80-1) and 223 µm to 323 µm (P60-2 and P80-2). Moreover, the connectivity was reduced from 4542 mm^{-1} to 376 mm^{-1} (P60-1 and P80-1) and from 4129 mm^{-1} to 603 mm^{-1} (P60-2 and P80-2).

In summary, increasing the level of the porogenic solvent (DMSO) and reducing the concentration of the polymerisation mixtures produced scaffolds with higher porosity and larger pores as well as giving a more open porosity and connectivity of the porous network.

3.1.5. Mechanical properties of the scaffolds

The indentation moduli for 4 percentages of strain were calculated for scaffolds P0, P60 and P80 with polymers 1, 2, 3 and 4 using a linear model for semi-infinite materials for 20% of the strain (Fig. S13 and Fig. 5). Scaffolds were cuboids with invariant dimensions (12 mm x 12 mm x 2 mm) for all polymer compositions and porosities.

Differences on the indentation moduli was observed as a result of the polymer composition (Fig. S14). Polymer P0-2 was observed to be significantly stiffer than polymer P0-1 ($p \leq 0.0001$), P0-3 ($p \leq 0.0001$) and P0-4 ($p \leq 0.001$). Moreover, significant difference was also observed between polymers P0-3 and P0-4 ($p \leq 0.01$). Among the four P0 polymers studied, polymer 2 showed the highest indentation moduli (40.3 ± 9.2 MPa) and polymer 3 the lowest (1.4 ± 0.3 MPa) between 0 to 5% strain. An increase in porogenic solvent levels (P60) produced a decrease of the indentation modulus for the

4 polymers between 0 to 5 % strain (Fig. 5B). For instance, polymer 2 changed from 40.3 ± 9.2 to 27.0 ± 7.9 MPa ($p \leq 0.01$) and polymer 3 from 1346.2 ± 334.5 to 57.2 ± 27.1 kPa ($p \leq 0.05$). A further drop of the indentation modulus was shown in the scaffolds with higher porosity (P80). In this case the indentation modulus for scaffolds P80-2 was 0.3 ± 0.1 MPa and for scaffolds P80-3 was 13.4 ± 7.2 kPa.

Relaxation load was also measured for 12 polymer scaffolds (Fig. 5C). Polymer 1 and 2 exhibited similar decreasing relaxation profile from P0 to P80. For example P0-1 and P80-1 changed from 35 ± 4% to 16 ± 3% ($p \leq 0.0001$) correspondingly. In the case of P0-2 and P80-2 relaxation loads were 43 ± 2% and 16 ± 4% ($p \leq 0.0001$) respectively. However, polymer 3 and 4 presented opposite increasing trend after 5 min. P0-3 and P80-3 changed from 5 ± 3% to 23 ± 4% ($p \leq 0.0001$). Moreover, scaffolds P0-4 and P80-4 displayed remarkable relaxation loads after 5 min with 45 ± 1% and 57 ± 4% ($p \leq 0.001$).

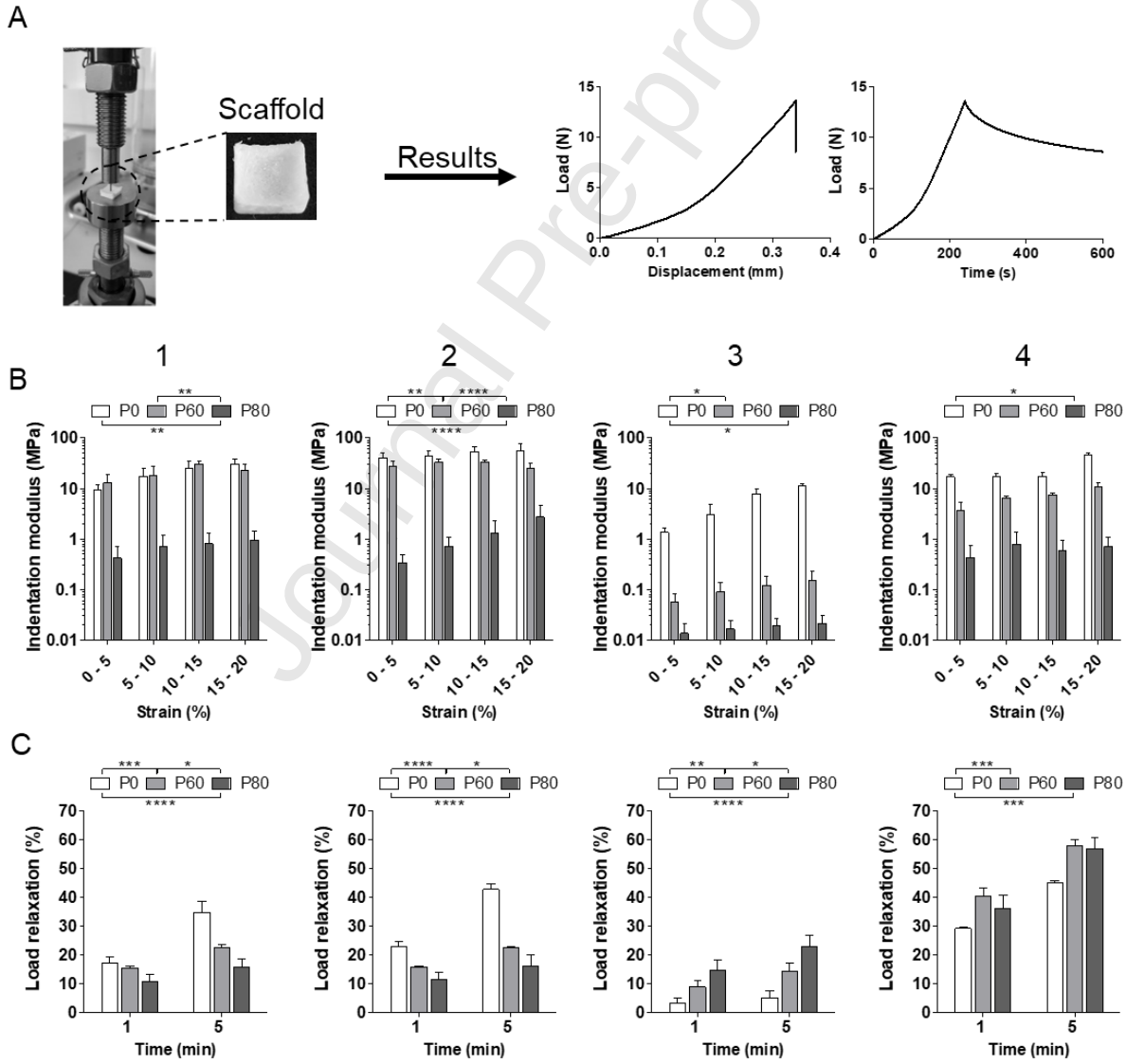

Figure 5. Mechanical properties of polymer scaffolds. *A) Macro-indentation approach to characterise mechanically the porous polymers using an Instron model 3367 equipped with a flat*

cylindrical indenter (Ø = 1 mm) for compression (e.g. load vs displacement or time for scaffold P0-1). The indentation modulus (E) was calculated locally using a linear model for semi-infinite media where the radius of the indenter (R) was fixed and the increment of the load (dF) vs displacement (dD) were calculated from the gradient of the curves of load vs displacement of each polymer. B) Indentation modulus for polymers 1, 2, 3 and 4 with low (P0), medium (P60) and high porosity (P80) at 4 different strain percentages. C) Load relaxation (%) after 1 and 5 min for polymers 1, 2, 3 and 4 with low, medium and high porosity. Statistics were calculated for the relaxation equilibrium (5 min). One-way ANOVA with Bonferroni post-test (p ≤ 0.05, ** p ≤ 0.01, *** p ≤ 0.001 and **** p ≤ 0.0001). Mean ± SD, n=4.*

3.2. In vitro evaluation of SAOS-2 on the scaffolds

3.2.1. Cell and polymer morphology by SEM.

Polymer microstructure and SAOS-2 cells morphology were analysed using SEM (Fig. 6). Polymer scaffold P60-1 and P80-1 were evaluated in the presence and absence of cells. Cells were observed to attach and cover the polymer surfaces after 3 days of incubation. Moreover, deposition of extracellular matrix was observed as well as some rounding up of cells on some scaffolds with poor attachment. In the case of the scaffolds with large porosity (P80), pores around 100 µm were observed to be populated with cells.

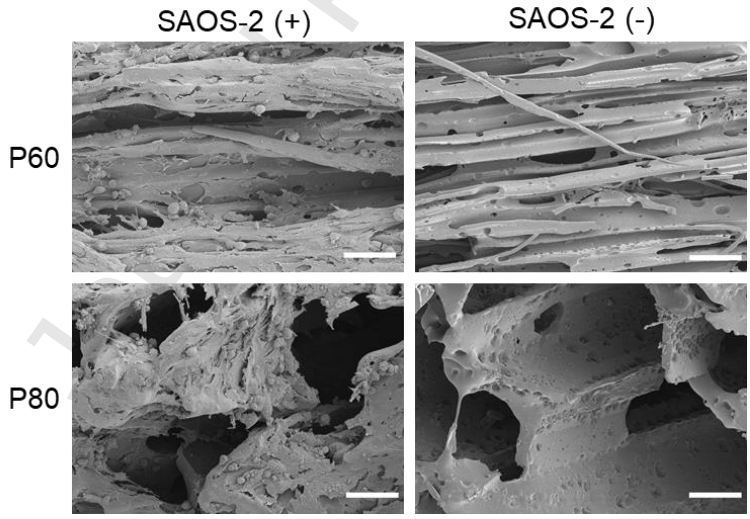

Figure 6. SEM images of the 3D polymers incubated with SAOS-2 cells. *Scaffolds of polymer 1 with medium (P60) and large (P80) porosity with (+) and without (-) SAOS-2 cells after 3 days of incubation. Scale bar 50 µm.*

3.2.2. Screening of SAOS-2 attachment and growth on the array of 3D polymer scaffolds

Screening of the scaffolds using SAOS-2 cells exposed the significant influence of polymer composition and 3D structure to cellular attachment and growth. SAOS-2 cell behaviour and the

population of viable cells on the polymers and tissue culture plates (control) was assessed using alamarBlue™ (Fig. 7). Normalised fluorescence intensity (NFI) was obtained as the ratio between the change of fluorescence intensity (as a result of resazurin reduction by the cells) in each scaffold to the plate control (TC) after 1 day of SAOS-2 cell seeding.

The effect of polymer composition on the number of cells attached was clearly observed in the P0 polymers. For example SAOS-2 cells growing on scaffolds P0-1, P0-2 and P0-4 did not show significant differences compared to cells grown on tissue culture plate whereas P0-3 supported lower number of cells compared with the same control ($p \leq 0.0001$). Moreover a decrease of the number of SAOS-2 cells was revealed when the porosity increased from P0 to P85. Among the 8 different polymer composition explored, polymer 2 was the only polymer composition capable of promoting cell proliferation between 1 and 7 days in 3D scaffolds. The normalised fluorescence intensity (NFI) for P60-2 changed from 0.9 ± 0.1 to 1.4 ± 0.1 ($p \leq 0.01$) from day 1 to 7 and from 0.6 ± 0.1 to 1.1 ± 0.1 ($p \leq 0.01$) for P80-2 in the same period of time. On the other hand, the number of SAOS-2 cells was stable for polymer 1 and a significant increase of cells was not observed. The relative ratio for P60-1 changed from 0.6 ± 0.1 to 0.7 ± 0.2 and in the case of P80-1 from 0.5 ± 0.1 to 0.7 ± 0.2.

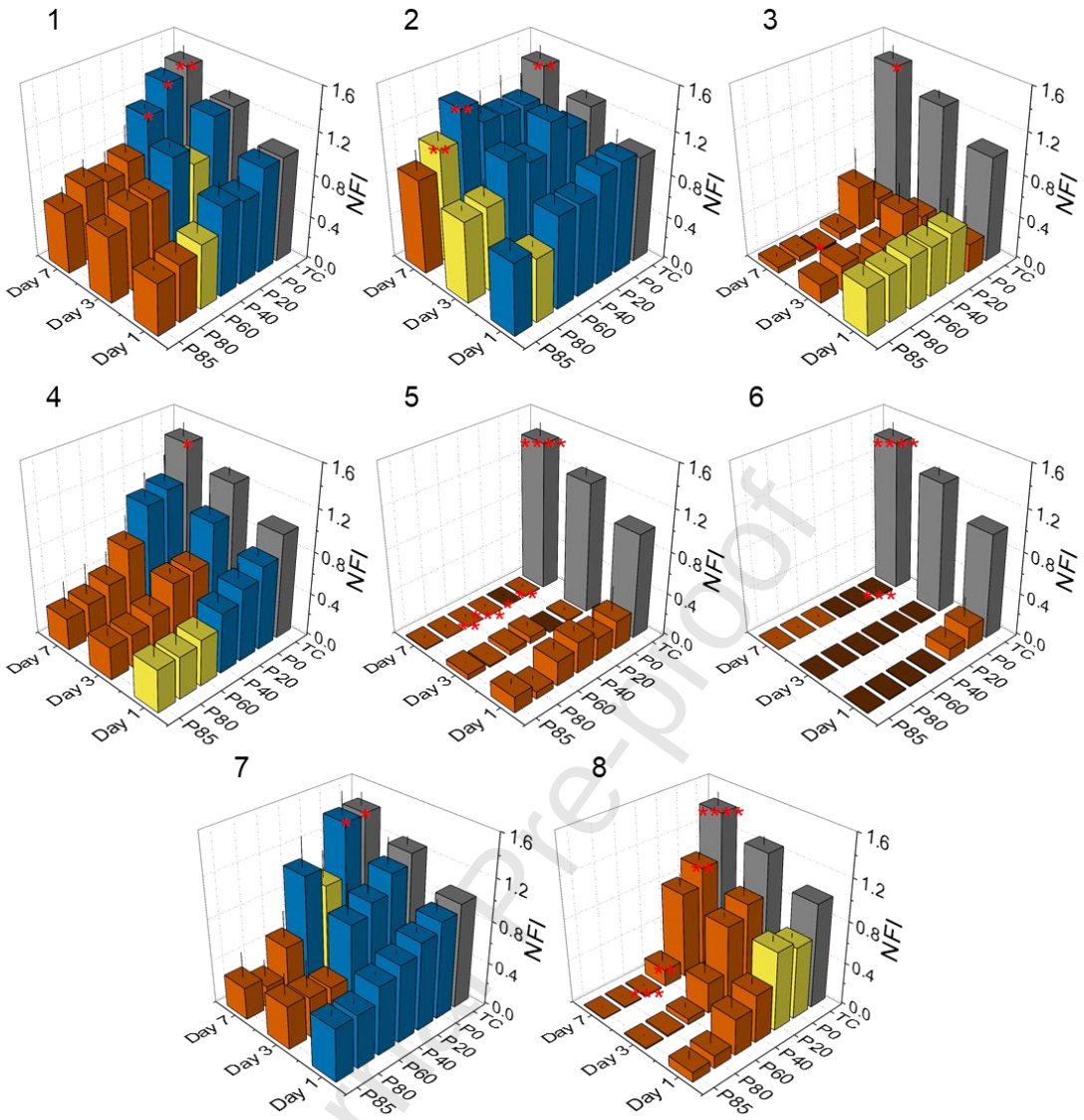

Figure 7. SAOS-2 viability over 7 days on the polymer scaffolds. *Normalised fluorescence intensity (NFI) between the cells seeded at day 1 in the tissue culture plate (TC, 20,000 SAOS-2/well) and at different time points (for the polymers 1, 2, 3, 4, 5, 6, 7 and 8) based on resazurin reduction (alamarBlue™). Two-way ANOVA with Bonferroni post-test between tissue culture plate and the different scaffolds (P0, P20, P40, P60, P80 and P85). Colour scale based on the significance of the differences to tissue culture plates; No differences (blue, p > 0.5), different (yellow, p ≤ 0.01) or very different (orange, p ≤ 0.0001). Two-way ANOVA with Bonferroni post-test between day 1 and day 7 (* p ≤ 0.05, ** p ≤ 0.01, *** p ≤ 0.001 and **** p ≤ 0.0001). Mean ± SD, n=3.*

3.2.3. SAOS-2 viability on the array of 3D polymer scaffolds

To support the above observations SAOS-2 cell viability on polymers 1 and 2 was assessed using a live/dead staining after 7 days of incubation with four levels of porosity (P0, P60, P80 and P85) studied (Fig. 8). Differences in cell attachment were observed between the non-porous polymers (P0-

1 and P0-2) and all the porous polymers (P60-1, P60-2, P80-1, P80-2, P85-1 and P85-2). Although cell attachment was found to be slightly enhanced in the non-porous controls there are several advantages of having the viable cells attached to the porous polymer structures in terms of having unrestricted apical-base polarity, efficient migration and nutrient exchange. The P60-2 scaffolds showed the highest cell density in the porous scaffolds. In the case of P80 and P85 scaffolds of polymer 1 and 2, the surface of the polymers were observed to be highly covered by live cells and the presence of cells in different layers of the porous scaffolds was observed (Fig. S17) which indicates that the 3D structure of the scaffolds were capable to arrange the cells in a hierarchical manner and maintain them in viable state over the experimental period of 7 days. For the polymer composition 1 and 2, a few dead cells were observed.

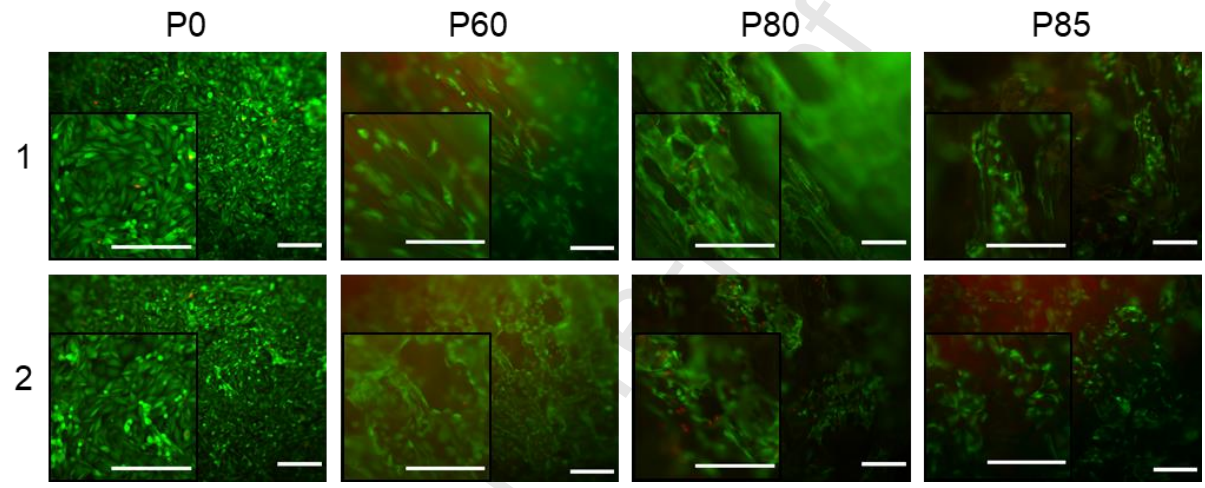

Figure 8. Live/dead staining of SAOS-2 cells on the array of 3D polymer scaffolds after 7 days in culture. *Polymer 1 (P0, P60, P80 and P85) and polymer 2 (P0, P60, P80 and P85). Live/dead staining - living cells (green) and dead cells (red). Scale bar 200 µm.*

3.2.4. SAOS-2 morphology in the 3D polymers

The 3D cell distribution in the scaffolds was studied together with the cytoskeleton orientation for the P60 and P80 scaffolds of polymers 1 and 2. Low cell spreading and rounded cells were observed for the P60 scaffolds whereas longitudinal cell spreading was detected in the P80 scaffolds (Fig. 9A). SAOS-2 cells were observed in different layers of the polymer structure (200 µm) after culture for 7 days in the P80 polymers. In contrast, poorer cell penetration into the polymer matrix was detected for the P60 scaffolds of polymers 1 and 2 with cells growing in an apparent “monolayer” on top of the porous scaffold (Video S2 and Video S3). Although cell penetration was about 15% of the height for P80 scaffolds, limitation of light penetration hinders the visualisation of the full 3D porous structure. The effect of the polymer microstructure on the orientation of the cell cytoskeleton was studied (using Imagej- OrientationJ). Colour maps suggested that cell cytoskeleton in P80 scaffolds were more oriented than P60 scaffolds of polymers 1 and 2 (Fig. 9B). Moreover, the quantification of the colour

maps also confirmed the prevalence of one main direction in the P80 scaffolds compared to P60 of polymer 1 and 2 (Fig. 9C).

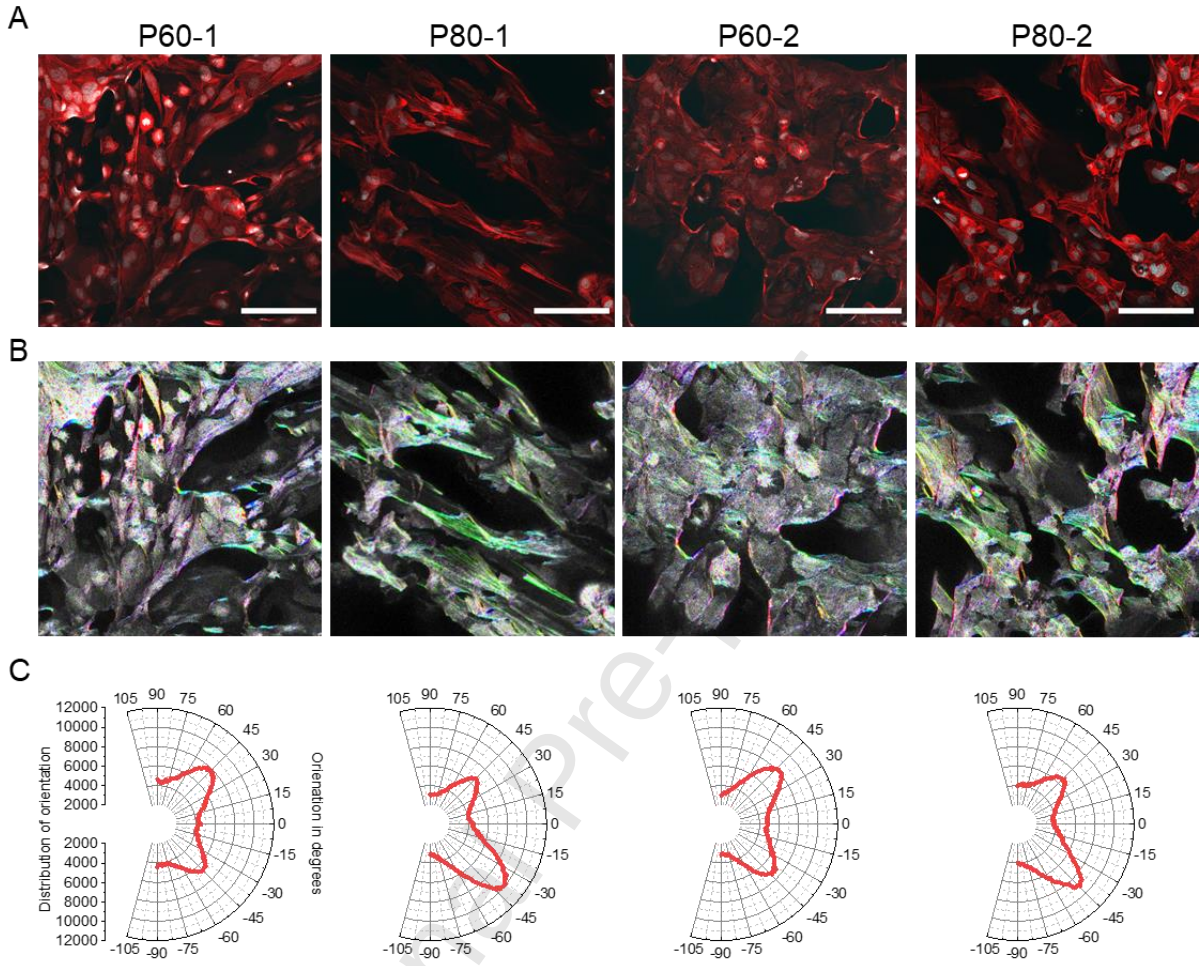

Figure 9. Analysis of the SAOS-2 cytoskeleton. *A) Representative images of the actin cytoskeleton of SAOS-2 in the polymers 1 and 2 with medium (P60) and high porosity (P80) after 7 days of incubation. Cell nucleus (cyan) and actin filaments (red). B) Colour map representing orientation of actin filaments encoded in color . C) Distribution of orientation formed by orientation analysis of every pixel of the image. Scale bar 100 µm.*

4. Discussion

Microarrays have been proven to be excellent tools to enable the non-biased discovery of new polymeric biomaterials. However, the limitations in terms of defined 3D structures offered on current array platforms impinges on its applicability within tissue engineering [40]. The development of an array of 3D polymer scaffolds was hence sought to expand the current scope of high-throughput methods to design and discover new functional polymers. The system developed demonstrated how the subtlest of tuning of the 3D architecture and stiffness of the polymer substrate can modify cell behaviour and allowed, from an array of 48 scaffolds, a potential candidate to be identified for

development of an in vitro bone model applicable in studying wide range of applications the development of bone models. Moreover, the tunability of the scaffold in addition to the parallel 3D morphological characterisation and the assessment of biological parameters permits the smart design of biomaterials.

Here freeze-casting was used to robustly generate various 3D porous structures, fabricated in a four steps process; preparation of the solutions, freezing, UV polymerisation and washing (Fig. 1) with homogenous heat transfer through the polypropylene well plate achieved using an aluminium cooling block. The UV polymerisation time was chosen to ensure total/completion of polymerisation of all the samples. Polyacrylates were used as the base architecture as they have shown application as a functional biomaterial, for instance, in controlling the growth of stem cells [17] and here eight different polyacrylates were explored (Table S1 and Fig. S1). Acrylate monomers and DMSO have been widely reported in the production of 3D scaffolds for biomedical applications *in vitro* as well as *in vivo* [38,41]. Moreover, the conversion during the polymerisation and the efficiency of the washing step to remove unreacted acrylate monomers was analysed by FTIR (Fig. S3). The reduction of temperature produced the formation of two phases; one rich-in-monomers and a rich-in-solvent. After UV polymerisation, the phase rich in solvent form the pores and the phase rich in monomers the polymer structure, although in the absence of cooling, small pores were also observed (Fig. S5) presumably as a consequence of polymerisation induced phase separation (cross-linked polymers became insoluble in the polymerisation mixture which produces segregation between the polymer network and the solvent [42]). These two mechanisms undoubtedly interplayed producing the formation of highly macroporous structures, with temperature also effecting polymer solubilisation. Sub-zero temperatures were selected to ensure that the DMSO remained in the frozen state during the photo-polymerisation and to allow efficient cooling gradients [41].

3D structures were successful controlled by the templating temperature and the concentration of the porogenic solvent (DMSO). The gradient of cooling was shown to be crucial for the formation of pores (Fig. 2). Among the 4 cooling procedures explored, a gradual change of temperature in the freezing step (during the so-called slow cooling process) produced scaffolds with the largest porosity and diameter of these pores and was selected as optimal. The effect of the quantity of porogenic solvent was also studied with scanning electron microscopy and Imagej-Fiji used to analyse the effect of the concentration of porogenic solvent on the porosity and Feret's diameter (Fig. 3). Increasing concentration of DMSO was shown to promote the formation of a porous 3D structure but little effect was observed in the size of these pores. The analysis of pore size distribution (Fig. S7) showed the presence of pore sizes from 100 µm to 300 µm, which could allow cells occupying the intraporous space forming 3D assemblies [43].

A high-throughput approach using micro-CT was developed to allow the single step high-content analysis of 12 polymer scaffolds at a time remarkably improving the understanding of the 3D morphological characteristics of the polymer scaffolds (Fig. S8 and Fig. S9). Control of the scaffold porosity with the concentration of porogenic solvent was proven using micro-CT and a liquid displacement method (Fig. 4C and Fig. S11-S12). Analysis of micro-CT also demonstrated 80% of

porogenic solvent (P80) produced the lowest levels of polymer connectivity density, the largest pore diameter and the most open porosity (Fig. 4D). Further increases of the concentration of porogenic solvent (P85) probably produced weakening and collapsing of part of the polymer network, reducing these properties in comparison to the P80 scaffolds. It was observed that the range of different 3D architectures developed matches the wide variety of 3D microenvironment of bones – for example the cortical section bone (the out layer of the bone) is characterised for its low cell density and porosity. On the other hand, the trabecular section is highly porous and vascularised with a higher density of cells [44].

The analysis of the indentation moduli allowed us to gain a deeper insight into the physical properties of the biomaterials with polymer composition and 3D structure were shown to determine the mechanical properties of the polymer scaffolds (Fig. 5). P0 and P60 scaffolds exhibited similar mechanical properties, however, P80 scaffolds presented an important reduction of the indentation stiffness. These differences were explained by changes of the ratio of DMSO to monomer as well as the 3D architecture of the polymer network. For instance, increase of the material stiffness was achieved by rising of the concentration of monomers in a polymerisation mixture [45,46], therefore, the increase of the concentration of DMSO in the polymerisation phase as a consequence of an incomplete phase separation during the freezing step could lead to softer scaffolds (P60 vs P80). Moreover, the phase separation produces orientation of the polymer structure and the formation of anisotropic materials, which increase scaffold stiffness in comparison to polymer chains which are more randomly distributed (P0 vs P60) [47]. In order to discern the effect of the porous structure in the mechanical properties of the polymer scaffolds, the indentation moduli were normalised with respect to their density which was measured with a method displacement approach (Fig. S15). The differences in the normalised indentation moduli between scaffolds P0 and P80 (Fig. S16) were revealed to be smaller than the observed in the original indentation moduli (Fig. 5), confirming that porosity was the main reason for stiffness reduction. The relaxation load has been shown to be an important property of tissues that undergo sustained stress (e.g. bone) [48]. The relaxation load for polymer scaffolds P80-2 varied from 16% to 43% after 5 min, which was within the range of the relaxation load previously reported for bones [49]. Overall, the mechanical properties of the polymers developed ranges from those of soft tissues such as kidneys or muscles (e.g. 6 and 16 kPa respectively) to collagenous bone (about 100 kPa) and mineralised bone (from 6 to 14 GPa) [31,46,50].

In order to shed light on the functionality of this novel array of 3D polymer scaffolds, it was applied to select porous biomaterials that were capable of mimicking the properties of bone e.g. open porous structure and stiff matrix [51–53] using osteosarcoma cells (SAOS-2) as in vitro model [54,55]. Integration of SAOS-2 within the polymer matrix was shown by SEM (Fig. 6) with cell attachment and matrix formation proven in the highly porous polymer structure for scaffolds P60 and P80 (of polymer 1). SAOS-2 maintenance and proliferation over 7 days with 8 different polymer composition and 6 levels of porosity were used to screen potential new biomaterials (Fig. 7).

From the potential 8 polymer compositions explored only polymer 2 was shown to be a candidate to generate a successful porous biomaterial. This polymer composition showed minimal differences in the number of cells compared with the control (tissue culture plate) and increase in these cells over 7 days (Fig. 7 – 2). By contrast, polymer 1 was capable of maintaining the cells alive for 7 days but proliferation was not detected (Fig. 7 – 1).

Polymer 1 and 2 were selected for further cell viability and scaffolds biocompatibility studies with live/dead staining showing high cell viability in the polymer scaffolds analysed (Fig. 8) with good consistency between alamarBlue™ and live/dead staining observed. Microscopy allowed live cell imaging of the 3D scaffolds, however, the presence of cells in different layers of the scaffolds and the uptake of the dyes by the porous polymers, as revealed by in vivo microscopy, shows one of the challenges of the approach (Fig. S17).

Distribution of SAOS-2 in 3D and the orientation of the cytoskeleton were studied in depth for the scaffolds P60 and P80 of polymer 1 and 2 (Fig. 9). Cells in different layers of the scaffold were detected for the polymers with the largest size of pores P80 in comparison with polymers with medium porosity P60 (Video S2 and Video S3). These two different polymer structures thus show the potential to obtain in vitro models for cortical or cancellous section of bones [44]. Moreover, the presence of a cytoskeleton orientation and the potential reorganisation of actin filaments (Fig. S18) that follow the polymers structure could promote differences in mechanotransduction mechanisms that potentially leads to differences cells behaviour [56].

The simultaneous comparison of SAOS-2 cells attachment and proliferation (viability day 1 and 7), scaffold stiffness and relaxation load in addition to 3D morphological analysis of the scaffolds allowed us to gain an understanding of cell-material interactions and the identification of successful candidatesfor development of a successful in vitro bone model which can be studied for multiple applications (Fig. 10). It has been observed here that maintaining a stiff substrate despite increasing porosity was crucial in the fabrication of 3D polymer scaffold as a consequence of the apparent dependence of SAOS-2 cells attachment and proliferation and the rigidity of the polymer. This is in accordance to earlier works where they report a similar behaviour [57,58].

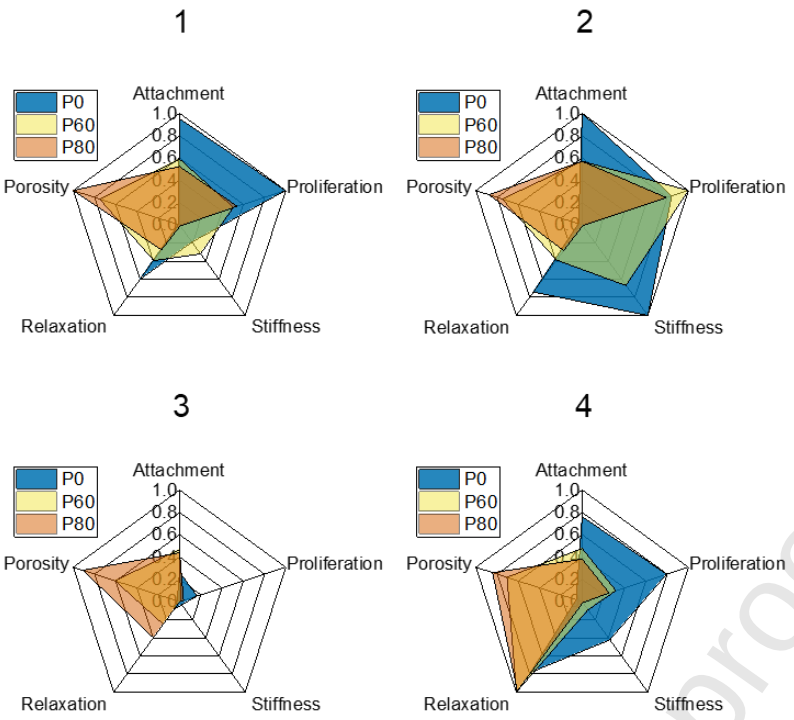

	Range (Max – Min)
Attachment (NFI)	1.1 – 0.3
Proliferation (NFI)	1.4 – 0.1
Stiffness (MPa – kPa)	40.3 – 13.4
Relaxation (%)	58.0 – 5.0
Porosity (%)	89.0 – 1.0

Figure 10. Graphic representation of the combined effect of the mechanical properties and porosity on the viability and proliferation of SAOS-2 cells. *Relative SAOS-2 cells attachment (NFI, day 1), proliferation (NFI, day 7), scaffold stiffness (MPa and kPa), load relaxation (%) and porosity (%) were calculated as value of these properties divided by the largest value of the characteristics interrogated for P0, P60 and P80 scaffolds of polymer 1, 2, 3 and 4.*

5. Conclusion

The structure, physical properties and chemical composition of 3D polymer scaffolds are conditioned simultaneously by the fabrication method and polymer choice. Differences in the 3D architecture and mechanical properties of biomaterials drive differences in cell behaviour and illustrates the need to fabricate arrays of 3D biomaterials to allow the successful discovery of functional materials. Arrays of 3D biomaterials were designed with the intention of merging the gap between 2D and 3D *in vitro* models. Here, a new multi-component and multi-mechanical properties array of polymer scaffolds was developed. The approach explored freeze-casting and gradients to fabricate simultaneously 48 scaffolds with different porous networks within a standard cell platform. This array of 3D polymer scaffolds expands the potential of the array approach to allow functional material identification. Characteristics of the pores were controlled through templating temperature/speed and concentration of the porogenic solvent. In addition, the concentration of the porogenic solvent tuned the mechanical characteristics of the scaffolds with a wide range of compressive properties. A high-throughput micro-CT approach was developed to allow detailed analysis of up to 12 scaffolds in a single scan. Biocompatibility of the polymers was studied using a proliferation assay and live/dead staining and the

effect of the polymer structure on the cytoskeleton of the cells explored. The scaffolds P60-2 and P80-2 promoted cell proliferation in a 3D environment and the open porous structure in a rigid polymer was shown to be comparable to the properties of bone. Moreover, the polymer structure could further lead to control of the organization of cells. Overall, the generation of arrays of 3D polymer scaffolds allowed a detailed study and understanding of the combined effect of polymer composition, 3D structure and mechanical properties on cellular behaviour as a step to select potential polymeric candidates for successful development of an in vitro bone model which can be used in a variety of scientific studies.

Disclosure

There are no conflicts of interests.

Acknowledgements

We thank the ERC (ERC-2013-ADG 340469 ADREEM) for funding and Mr Stephen Mitchell for his technical support and helpful advice in scanning electron microscopy (Biology scanning EM facility – University of Edinburgh).

6. References

[1] L.G. Griffith, M.A. Swartz, Capturing complex 3D tissue physiology in vitro., Nat. Rev. Mol. Cell Biol. 7 (2006) 211–24. doi:10.1038/nrm1858.

[2] K. Duval, H. Grover, L.-H. Han, Y. Mou, A.F. Pegoraro, J. Fredberg, Z. Chen, Modeling Physiological Events in 2D vs. 3D Cell Culture, Physiology. 32 (2017) 266–277. doi:10.1152/physiol.00036.2016.

[3] P. Zorlutuna, N. Annabi, G. Camci-Unal, M. Nikkhah, J.M. Cha, J.W. Nichol, A. Manbachi, H. Bae, S. Chen, A. Khademhosseini, Microfabricated biomaterials for engineering 3D tissues, Adv. Mater. 24 (2012) 1782–1804. doi:10.1002/adma.201104631.

[4] A. Atala, F. Kasper, A. Mikos, Engineering Complex Tissues, Sci. Transl. Med. 4 (2012) 160rv12.

[5] D.E. Discher, P. Janmey, Y.-L. Wang, Tissue cells feel and respond to the stiffness of their substrate., Science. 310 (2005) 1139–43. doi:10.1126/science.1116995.

[6] V. Karageorgiou, D. Kaplan, Porosity of 3D biomaterial scaffolds and osteogenesis, Biomaterials. 26 (2005) 5474–5491. doi:10.1016/j.biomaterials.2005.02.002.

[7] J.H. Wen, L.G. Vincent, A. Fuhrmann, Y.S. Choi, K.C. Hribar, H. Taylor-Weiner, S. Chen, A.J. Engler, Interplay of matrix stiffness and protein tethering in stem cell differentiation, Nat. Mater. advance on (2014) 1–21. doi:10.1038/nmat4051.

[8] H. Liu, J. Usprech, Y. Sun, C.A. Simmons, A microfabricated platform with hydrogel arrays for

3D mechanical stimulation of cells, ACTA Biomater. 34 (2016) 113–124. doi:10.1016/j.actbio.2015.11.054.

[9] N.N.T. Le, S. Zorn, S.K. Schmitt, P. Gopalan, W.L. Murphy, Hydrogel arrays formed via differential wettability patterning enable combinatorial screening of stem cell behavior, Acta Biomater. 34 (2015) 93–103. doi:10.1016/j.actbio.2015.09.019.

[10] S.H. Oh, D.B. An, T.H. Kim, J.H. Lee, Wide-range stiffness gradient PVA/HA hydrogel to investigate stem cell differentiation behavior, Acta Biomater. 35 (2016) 23–31. doi:10.1016/j.actbio.2016.02.016.

[11] A. Hansen, R. Zhang, M. Bradley, Fabrication of arrays of polymer gradients using inkjet printing, Macromol. Rapid Commun. 33 (2012) 1114–1118. doi:10.1002/marc.201200193.

[12] G. Rijal, W. Li, A versatile 3D tissue matrix scaffold system for tumor modeling and drug screening, Sci. Adv. 3 (2017) 1–17. doi:10.1126/sciadv.1700764.

[13] R. Edri, I. Gal, N. Noor, T. Harel, S. Fleischer, N. Adadi, O. Green, D. Shabat, L. Heller, A. Shapira, I. Gat-Viks, D. Peer, T. Dvir, Personalized Hydrogels for Engineering Diverse Fully Autologous Tissue Implants, Adv. Mater. 31 (2019) 1–9. doi:10.1002/adma.201803895.

[14] F. Khan, R.S. Tare, R.O.C. Oreffo, M. Bradley, Versatile biocompatible polymer hydrogels: Scaffolds for cell growth, Angew. Chemie - Int. Ed. 48 (2009) 978–982. doi:10.1002/anie.200804096.

[15] J.J. Hanak, The “multiple-sample concept” in materials research: Synthesis, compositional analysis and testing of entire multicomponent systems, J. Mater. Sci. 5 (1970) 964–971. doi:10.1007/BF00558177.

[16] G. Tourniaire, J. Collins, S. Campbell, H. Mizomoto, S. Ogawa, J.F. Thaburet, M. Bradley, Polymer microarrays for cellular adhesion, Chem. Commun. (2006) 2118–2120. doi:10.1039/b602009g.

[17] A. Hansen, H.K. Mjoseng, R. Zhang, M. Kalloudis, V. Koutsos, P.A. de Sousa, M. Bradley, High-Density Polymer Microarrays: Identifying Synthetic Polymers that Control Human Embryonic Stem Cell Growth, Adv. Healthc. Mater. 3 (2014) 848–853. doi:10.1002/adhm.201300489.

[18] A. Ranga, S. Gobaa, Y. Okawa, K. Mosiewicz, A. Negro, M.P. Lutolf, 3D niche microarrays for systems-level analyses of cell fate, Nat. Commun. 5 (2014) 1–10. doi:10.1038/ncomms5324.

[19] A.K. Gaharwar, A. Arpanaei, T.L. Andresen, 3D Biomaterial Microarrays for Regenerative Medicine : Current State-of-the-Art , Emerging Directions and Future Trends, Adv. Mater. 28 (2016) 771–781. doi:10.1002/adma.201503918.

[20] C. Duffy, A. Venturato, A. Callanan, A. Lilienkampf, M. Bradley, Arrays of 3D double-network hydrogels for the high-throughput discovery of materials with enhanced physical and biological

properties, Acta Biomater. 34 (2016) 104–112. doi:10.1016/j.actbio.2015.12.030.

[21] K. Cheng, Y. Lai, W.S. Kisaalita, Three-dimensional polymer scaffolds for high throughput cell-based assay systems, Biomaterials. 29 (2008) 2802–2812. doi:10.1016/j.biomaterials.2008.03.015.

[22] Y. Yang, D. Bolikal, M.L. Becker, J. Kohn, D.N. Zeiger, C.G. Simon, Combinatorial polymer scaffold libraries for screening cell-biomaterial interactions in 3D, Adv. Mater. 20 (2008) 2037–2043. doi:10.1002/adma.200702088.

[23] X. Yan, L. Zhou, Z. Wu, X. Wang, X. Chen, F. Yang, Y. Guo, M. Wu, Y. Chen, W. Li, J. Wang, Y. Du, High throughput scaffold-based 3D micro-tumor array for efficient drug screening and chemosensitivity testing, Biomaterials. (2018) 1–13. doi:10.1016/j.biomaterials.2018.05.020.

[24] B. Thavornyutikarn, N. Chantarapanich, K. Sitthiseripratip, G.A. Thouas, Q. Chen, Bone tissue engineering scaffolding: computer-aided scaffolding techniques, 2014. doi:10.1007/s40204-014-0026-7.

[25] W.L. Li, K. Lu, J.Y. Walz, Freeze casting of porous materials: review of critical factors in microstructure evolution, Int. Mater. Rev. 57 (2011) 37–60. doi:10.1179/1743280411y.0000000011.

[26] I.A. Quintero Ortega, J.D. Mota-Morales, E.A. Elizalde Peña, D.G. Zárate-Triviño, Y.A. De Santiago, A. Ortiz, B. García Gaitan, I.C. Sanchez, G. Luna-Bárcenas, Cryogenic process to elaborate poly(ethylene glycol) scaffolds. Experimental and simulation studies, Ind. Eng. Chem. Res. 52 (2013) 706–715. doi:10.1021/ie301441j.

[27] H. Bai, D. Wang, B. Delattre, W. Gao, J. De Coninck, S. Li, A.P. Tomsia, Biomimetic gradient scaffold from ice-templating for self-seeding of cells with capillary effect, Acta Biomater. 20 (2015) 113–119. doi:10.1016/j.actbio.2015.04.007.

[28] S. Christoph, A. Hamraoui, E. Bonnin, C. Garnier, T. Coradin, F.M. Fernandes, Ice-templating beet-root pectin foams: Controlling texture, mechanics and capillary properties, Chem. Eng. J. 350 (2018) 20–28. doi:10.1016/j.cej.2018.05.160.

[29] M. Doube, M.M. Klosowski, I. Arganda-Carreras, F.P. Cordelières, R.P. Dougherty, J.S. Jackson, B. Schmid, J.R. Hutchinson, S.J. Shefelbine, BoneJ: Free and extensible bone image analysis in ImageJ, Bone. 47 (2010) 1076–1079. doi:10.1016/j.bone.2010.08.023.

[30] J.N.G. S.P. Timoshenko, Theory of Elasticity. Chapter 1, in: McGraw-Hill (Ed.), Theory Elast., 3rd ed., 1951: pp. 1–14.

[31] V. Egorov, S. Tsyuryupa, S. Kanilo, M. Kogit, A. Sarvazyan, Soft tissue elastometer, Med. Eng. Phys. 30 (2008) 206–212. doi:10.1016/j.medengphy.2007.02.007.

[32] R.M. Delaine-Smith, S. Burney, F.R. Balkwill, M.M. Knight, Experimental validation of a flat punch indentation methodology calibrated against unconfined compression tests for

determination of soft tissue biomechanics, J. Mech. Behav. Biomed. Mater. 60 (2016) 401–415. doi:10.1016/j.jmbbm.2016.02.019.

[33] S.D. McCullen, H. Autefage, A. Callanan, E. Gentleman, M.M. Stevens, Anisotropic Fibrous Scaffolds for Articular Cartilage Regeneration, Tissue Eng. Part A. 18 (2012) 2073–2083. doi:10.1089/ten.tea.2011.0606.

[34] J.A.M. Steele, S.D. McCullen, A. Callanan, H. Autefage, M.A. Accardi, D. Dini, M.M. Stevens, Combinatorial scaffold morphologies for zonal articular cartilage engineering, Acta Biomater. 10 (2014) 2065–2075. doi:10.1016/j.actbio.2013.12.030.

[35] R. Rezakhaniha, A. Agianniotis, J.T.C. Schrauwen, A. Griffa, D. Sage, C.V.C. Bouten, F.N. Van De Vosse, M. Unser, N. Stergiopulos, Experimental investigation of collagen waviness and orientation in the arterial adventitia using confocal laser scanning microscopy, Biomech. Model. Mechanobiol. 11 (2012) 461–473. doi:10.1007/s10237-011-0325-z.

[36] E. López-Ruiz, S. Venkateswaran, M. Perán, G. Jiménez, S. Pernagallo, J.J. Díaz-Mochón, O. Tura-Ceide, F. Arrebola, J. Melchor, J. Soto, G. Rus, P.J. Real, M. Dlaz-Ricart, A. Conde-González, M. Bradley, J.A. Marchal, Poly(ethylmethacrylate-co-diethylaminoethyl acrylate) coating improves endothelial re-population, bio-mechanical and anti-thrombogenic properties of decellularized carotid arteries for blood vessel replacement, Sci. Rep. 7 (2017) 1–14. doi:10.1038/s41598-017-00294-6.

[37] R. Santoro, S. Venkateswaran, F. Amadeo, R. Zhang, M. Brioschi, A. Callanan, M. Agrifoglio, C. Banfi, M. Bradley, M. Pesce, Acrylate-based materials for heart valve scaffold engineering, Biomater. Sci. 6 (2018) 154–167. doi:10.1039/c7bm00854f.

[38] G. Jiménez, S. Venkateswaran, E. López-Ruiz, M. Perán, S. Pernagallo, J.J. Díaz-Monchón, R.F. Canadas, C. Antich, J.M. Oliveira, A. Callanan, R. Walllace, R.L. Reis, E. Montañez, E. Carrillo, M. Bradley, J.A. Marchal, A soft 3D polyacrylate hydrogel recapitulates the cartilage niche and allows growth-factor free tissue engineering of human articular cartilage, Acta Biomater. 90 (2019) 146–156. doi:10.1016/j.actbio.2019.03.040.

[39] R.A. Perez, G. Mestres, Role of pore size and morphology in musculo-skeletal tissue regeneration, Mater. Sci. Eng. C. 61 (2016) 922–939. doi:10.1016/j.msec.2015.12.087.

[40] K.E. Sung, X. Su, E. Berthier, C. Pehlke, A. Friedl, D.J. Beebe, Understanding the Impact of 2D and 3D Fibroblast Cultures on In Vitro Breast Cancer Models, PLoS One. 8 (2013) 1–13. doi:10.1371/journal.pone.0076373.

[41] S. Jiang, C. Lyu, P. Zhao, W. Li, W. Kong, C. Huang, G.M. Genin, Y. Du, Cryoprotectant enables structural control of porous scaffolds for exploration of cellular mechano-responsiveness in 3D, Nat. Commun. 10 (2019). doi:10.1038/s41467-019-11397-1.

[42] D.L. Elbert, Liquid-liquid two-phase systems for the production of porous hydrogels and hydrogel microspheres for biomedical applications: A tutorial review, Acta Biomater. 7 (2011)

31–56. doi:10.1016/j.actbio.2010.07.028.

[43] C.M. Murphy, M.G. Haugh, F.J. O'Brien, The effect of mean pore size on cell attachment, proliferation and migration in collagen-glycosaminoglycan scaffolds for bone tissue engineering, Biomaterials. 31 (2010) 461–466. doi:10.1016/j.biomaterials.2009.09.063.

[44] H. Follet, G. Boivin, C. Rumelhart, P.J. Meunier, The degree of mineralization is a determinant of bone strength: A study on human calcanei, Bone. 34 (2004) 783–789. doi:10.1016/j.bone.2003.12.012.

[45] X. Jiang, P.C. Georges, B. Li, Y. Du, M.K. Kutzing, M.L. Previtera, N.A. Langrana, B.L. Firestein, Cell Growth in Response to Mechanical Stiffness is Affected by Neuron- Astroglia Interactions, Open Neurosci. J. 1 (2007) 7–14. doi:10.2174/1874082000701010007.

[46] A.K. Denisin, B.L. Pruitt, Tuning the Range of Polyacrylamide Gel Stiffness for Mechanobiology Applications, ACS Appl. Mater. Interfaces. 8 (2016) 21893–21902. doi:10.1021/acsami.5b09344.

[47] H. Bai, Y. Chen, B. Delattre, A.P. Tomsia, R.O. Ritchie, Bioinspired large-scale aligned porous materials assembled with dual temperature gradients, Sci. Adv. 1 (2015) e1500849. doi:10.1126/sciadv.1500849.

[48] X. Liang, J. Gao, W. Xu, X. Wang, Y. Shen, J. Tang, S. Cui, X. Yang, Q. Liu, L. Yu, J. Ding, Structural mechanics of 3D-printed poly(lactic acid) scaffolds with tetragonal, hexagonal and wheel-like designs, Biofabrication. 11 (2019) 035009. doi:10.1088/1758-5090/ab0f59.

[49] D.D. Deligianni, A. Maris, Y.F. Missirlis, Stress relaxation behaviour of trabecular bone specimens, J. Biomech. 27 (1994) 1469–1476. doi:10.1016/0021-9290(94)90196-1.

[50] A.J. Engler, S. Sen, H.L. Sweeney, D.E. Discher, Matrix Elasticity Directs Stem Cell Lineage Specification, Cell. 126 (2006) 677–689. doi:10.1016/j.cell.2006.06.044.

[51] F. Khan, R.S. Tare, J.M. Kanczler, R.O.C. Oreffo, M. Bradley, Strategies for cell manipulation and skeletal tissue engineering using high-throughput polymer blend formulation and microarray techniques, Biomaterials. 31 (2010) 2216–2228. doi:10.1016/j.biomaterials.2009.11.101.

[52] F. Khan, J.O. Smith, J.M. Kanczler, R.S. Tare, R.O.C. Oreffo, M. Bradley, Discovery and evaluation of a functional ternary polymer blend for bone repair: Translation from a microarray to a clinical model, Adv. Funct. Mater. 23 (2013) 2850–2862. doi:10.1002/adfm.201202710.

[53] D.L. Lopes, C. Martins-Cruz, M.B. Oliveira, J.F. Mano, Bone Physiology as Inspiration for Tissue Regenerative Therapies, Biomaterials. 185 (2018) 240–275. doi:10.1016/j.biomaterials.2018.09.028.

[54] S.B. Rodan, Y. Imai, M.A. Thiede, G. Wesolowski, D. Thompson, Z. Bar-Shavit, S. Shull, K. Mann, G.A. Rodan, Characterization of a Human Osteosarcoma Cell Line (Saos-2) with

Osteoblastic Properties, Cancer Res. 47 (1987) 4961–4966.

[55] M. Prideaux, A.R. Wijenayaka, D.D. Kumarasinghe, R.T. Ormsby, A. Evdokiou, D.M. Findlay, G.J. Atkins, SaOS2 osteosarcoma cells as an in vitro model for studying the transition of human osteoblasts to osteocytes, Calcif. Tissue Int. 95 (2014) 183–193. doi:10.1007/s00223-014-9879-y.

[56] K.A. Kilian, B. Bugarija, B.T. Lahn, M. Mrksich, Geometric cues for directing the differentiation of mesenchymal stem cells., Proc. Natl. Acad. Sci. U. S. A. 107 (2010) 4872–7. doi:10.1073/pnas.0903269107.

[57] N.D. Leipzig, M.S. Shoichet, The effect of substrate stiffness on adult neural stem cell behavior, Biomaterials. 30 (2009) 6867–6878. doi:10.1016/j.biomaterials.2009.09.002.

[58] G.J. Her, H.C. Wu, M.H. Chen, M.Y. Chen, S.C. Chang, T.W. Wang, Control of three-dimensional substrate stiffness to manipulate mesenchymal stem cell fate toward neuronal or glial lineages, Acta Biomater. 9 (2013) 5170–5180. doi:10.1016/j.actbio.2012.10.012.

Graphical abstract

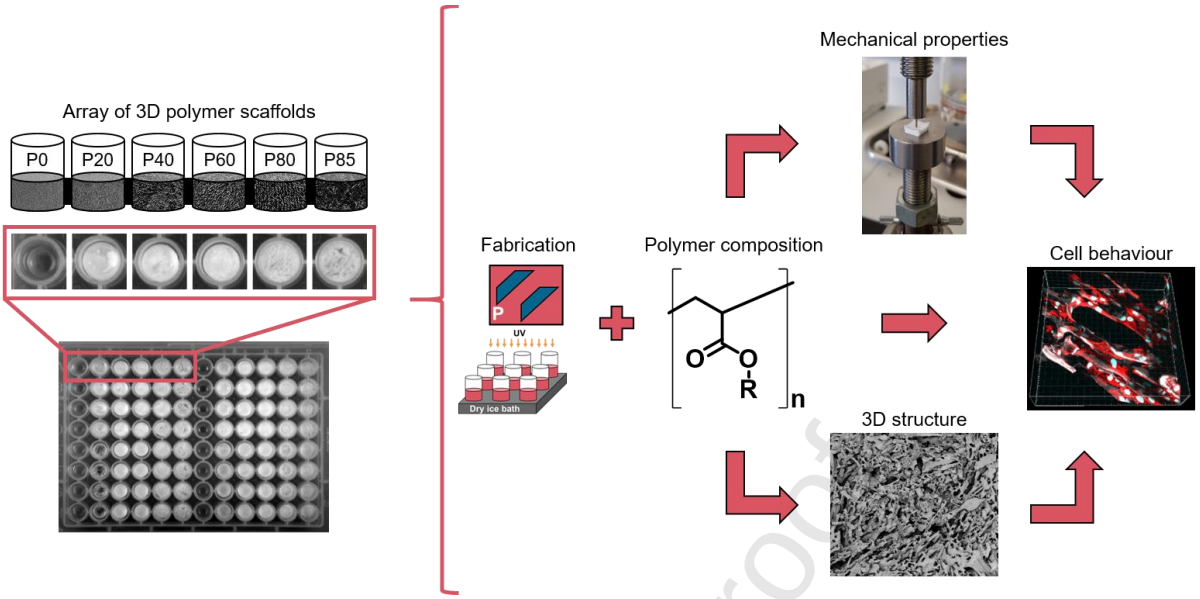

Highlights

- The development of an array of 3D polymer scaffolds.
- Multi-material and multi-structure scaffolds efficiently fabricated using a high-throughput approach *via* freeze-casting and photo-polymerisation.
- High-throughput structural characterisation of the porous scaffolds including a novel parallel micro-CT analysis approach.
- Array of porous scaffolds facilitates the analysis of 3D of cell-material interactions and the identification of functional polymer scaffolds.